Domain wall pinning and domain wall resistivity in notched $La_{0.7}Sr_{0.3}MnO_3$ nanostructures

Junxiang, Yao; Geenen, Maurits E.K.; Bakker, Harm A.; Abelmann, Leon; Aarts, Jan

Important note
To cite this publication, please use the final published version (if applicable).
Please check the document version above.

Domain wall pinning and domain wall resistivity in notched La$_{0.7}$Sr$_{0.3}$MnO$_3$ nanostructures

Yao Junxiang,[1,*] Maurits E. K. Geenen,[1] Harm A. Bakker ●,[2] Leon Abelmann,[3] and Jan Aarts ●[1,†]

[1]*Huygens-Kamerlingh Onnes Laboratory, Leiden Institute of Physics, Leiden University. P.O. Box 9504, 2300 RA Leiden, The Netherlands*
[2]*MESA+ Institute for Nanotechnology, University of Twente, P.O. Box 217, 7500 AE Enschede, The Netherlands*
[3]*Department of microelectronics, Technical University Delft, Mekelweg 4, 2628 CD Delft, The Netherlands*

Creation and manipulation of magnetic domain walls (DWs) are a core subject of research in developing prototype devices for spintronic applications. DWs can be created artificially and moved by applying either a magnetic field or an electric current, as has been extensively investigated. Here, we study the DW pinning and depinning in half-metallic ferromagnetic La$_{0.7}$Sr$_{0.3}$MnO$_3$ nanostructures with a notch that is about 90% of the width of the wire. By measuring the magnetoresistance of the notched wires while sweeping the magnetic field, we unambiguously observe DW pinning and depinning from 10 to 300 K. Analysis of the temperature dependence reveals that both ΔR (the DW resistance) and $\Delta R/R_0$ (R_0 is the resistance at zero field) are proportional to the temperature. The DW resistivity is calculated to be of the order of $10^{-17}\,\Omega\,m^2$ at 10 K and $10^{-15}\,\Omega\,m^2$ at 300 K. The latter value agrees with the reported intrinsic DW resistivity in films. In addition, we find approximately constant ΔR and $\Delta R/R_0$ for widths from 5 down to 1.8 μm and a pronounced increase in both quantities when the width goes down to 755 nm. With the extracted magnetocrystalline anisotropy parameters from the measurements of the remanent magnetization and the magnetic torque as function of angle of the magnetic field with respect to the substrate normal, we further perform micromagnetic simulations and obtain results consistent with the experimental data. Our work may promote designing relevant prototypes and may constitute a platform to explore the effect of spin torque transfer on DWs.

I. INTRODUCTION

Spin structures, in the form of skyrmions [1], vortex textures [2], magnetic domain walls [3], three-dimensional nanomagnetism [4], etc., hold promise for potential applications in future spintronic devices. In particular, magnetic domain walls (DWs) have been extensively studied during the last few decades. A DW is a topological spin structure that spontaneously forms in ferromagnetic bulk materials as a result of the energy competition between various magnetic interactions. Magnetic fields and electric pulses have been proven to be able to move DWs effectively, which may pave the way toward nonvolatile memories and logic circuits hence has led to continuing research interest [5].

In order to satisfy the requirements of applicability and high integration, many efforts have been made to create and control DWs on the nanoscale. The formation of DWs is the result of an energy compromise among various energy terms, i.e., exchange energy, Zeeman energy, demagnetization energy, etc., involved in a ferromagnet. An effective method to control the energy competition is to utilize shape anisotropy, which is commonly used in constructing a desired DW on the nanoscale. Hayashi *et al.* created four different metastable DW states (discernable by different changes in the resistance for the different states) by introducing a shallow notch into a Ni$_{80}$Fe$_{20}$ permalloy (Py) nanostructure [6]. These states were either a simple transverse DW (TDW) or a more complicated vortex DW (VDW), which could reside either in or to the side of the notch. The data revealed that a VDW could transform into a TDW when passing through the notch. The chirality of the DW can also be distinguished by measuring the magnetoresistance (MR). Moreover, Kim *et al.* realized synchronous motion of TDWs using magnetic field pulses in the design involving a series of triangular notches with a certain spacing [7].

DW motion can be driven by applying an external magnetic field or a spin-polarized electric current [8–10]. Previous studies demonstrated that the threshold current for motion J_c is on the order of 10^{12} A/m^2 in the case of, e.g., Co, Py, and Fe, which are not fully spin polarized and hence provide a less-than-optimal spin transfer torque (STT) [11,12]. As a comparison, half-metallic ferromagnets (HMFs), in which only one spin channel is present, hold the promise for lowering J_c significantly. Several attempts have been made to study the DW pinning and depinning in HMFs, in particular in CrO$_2$ and various manganite oxides. Chen *et al.* observed the stable creation and annihilation of DW-like spin textures in devices with constrictions by measuring the resistance jump when catching the DW with a field sweep [13]. Their

*Contact author: yao@Physics.LeidenUniv.nl
†Contact author: aarts@Physics.LeidenUniv.nl

analysis further revealed a large spin asymmetry ratio in the CrO_2 nanostructure. In another work, J_c to alter the magnetic configuration of a CrO_2 nanowire was found to be on the order of 10^{10} A/m^2 [14]. Despite a possible contribution by the current-induced Joule heating at low temperatures, the required J_c for DW motion in CrO_2 is 2 orders smaller than that in conventional ferromagnets, indicating the high efficiency of STT in HMFs. However, the strong magnetocrystalline anisotropy of epitaxial CrO_2 hinders controllable manipulation of DWs and the corresponding practical application.

Alternatively, manganite oxides, i.e., $La_{0.7}Ca_{0.3}MnO_3$ (LCMO) and $La_{0.7}Sr_{0.3}MnO_3$ (LSMO), are suitable candidates for investigating DWs due to their weak magnetocrystalline anisotropy, which can be modulated artificially by using a variety of substrates [15]. Therefore, shape anisotropy appears to be quite effective in tailoring DWs in the nanostructured manganite oxides. Ruotolo *et al.* demonstrated the creation of a DW in a double-notched LSMO nanostructure, as well as reversible DW pinning and depinning enabled by using either the magnetic field or electric current at low temperature [16]. Wang *et al.* reported striped DW motion in a thin film driven by a small J_c ($\sim 10^8$ A/m^2) due to the efficient STT in the film, suggesting the possibility of electric current control of the spin structure in an LSMO-based device [17,18]. However, a more systematic study of DW creation and annihilation in a notched LSMO nanostructure has not been reported. One issue that needs consideration in such a study is that of electronic phase separation that may occur locally in nanostructures of manganite oxides, which can give rise to uncontrolled devices [19–21].

In this work, we investigate the DW pinning and depinning in notched LSMO bar-shaped nanostructures that are attached to an LSMO pad as the source for DWs and tapered at the end. By sweeping the magnetic field and measuring the MR simultaneously, we unambiguously observe stable DW pinning and depinning in devices with different widths and notch depths. Analysis of the temperature dependence further demonstrates that DWs can be pinned and depinned from 10 to 300 K. We compare our findings, in particular the values of the pinning field H_{pin}, with earlier work on CrO_2 and LSMO nanostructures. We also estimate the DW resistivity (actually the resistance-area product) and find it to be on the order of 10^{-17} Ω m^2 at 10 K and 10^{-15} Ω m^2 at 300 K, in agreement with estimates from other types of experiments. Additionally, we perform micromagnetic simulations using magnetic anisotropy constants that were extracted from field-angle-dependent magnetic torque measurements. The simulated results demonstrate magnetic behavior that is consistent with our experimental observations.

II. EXPERIMENTAL METHODS

Thin films were grown epitaxially on a (001)-oriented $(LaAlO_3)_{0.3}(Sr_2TaAlO_6)_{0.7}$ (LSAT) substrate (5×5 mm^2), chosen for its small lattice mismatch with LSMO (roughly -0.2%), which results in only weak magnetocrystalline anisotropy [22]. We used an off-axis sputtering system described previously in Ref. [23]. In the sputtering chamber, the working distances were 75 mm from the surface of the heater to the axis of the target and 45 mm from the surface of the

target to the axis of the heater. The growth temperature was 700 °C, and the deposition pressure was kept at 0.7 mbar by flowing a mix of argon and oxygen gas (3:2). The sputtering power was 50 W. After a nominal 10 nm LSMO thin film was grown, the temperature was gradually decreased to room temperature (RT) at a rate of 25 °C/min while the sputter pressure was maintained. We employed extensive methods to examine the properties of the LSMO thin films, in particular confirming the perfect epitaxy of LSMO on LSAT [24]. Next, electron beam lithography and Ar-ion beam etching were utilized to pattern the LSMO thin film into a series of notched LSMO nanostructures with a pad on one end and a wire with a fixed length of 50 μm and varying widths, i.e., 0.76, 1.8, 2.8, and 4.9 μm. The notches were kept at a constant *relative* depth of 90%. To form electrical leads, Pt contacts with a thickness of 50 nm were fabricated using a standard diode sputtering system and liftoff. Devices were connected by bonding the Pt leads to an electronic board using Al wires, forming a four-probe configuration, as schematically depicted in the false-color scanning electron microscopy (SEM) image in Fig. 1(a). The current was applied to the outer two Pt leads, while the inner two leads were used as voltage probes. The devices were measured in a physical property measurement system (Quantum Design), which provides a measurement environment with accurately adjustable temperature and field. In order to characterize the magnetic properties of LSMO, continuous films were measured with a DMS VSM-10 vibrating sample magnetometer (VSM). The sample size was 5×5 mm^2. The system was calibrated with Ni foil of identical size and a known weight using the literature value for the saturation magnetization of Ni (55.1 A m^2/kg) [25]. The diamagnetic contribution of the sample holder was subtracted as a linear background signal of (-0.24 ± 0.02) nA m^2/mT, obtained with a fit to the high-field branches of the in-plane hysteresis loops. The magnetic signal of the combined sample holder plus the bare substrate was on the order of 0.01 μA m^2, which is about 5% of the saturation magnetization of the 10 nm film $(0.19 \pm 0.01$ μA m$^2)$. As a matter of fact, we can use the measured saturation magnetization to calculate the film thickness t and find $t = 12.5$ nm.

III. RESULTS

Here, we focus on the nanostructure with a width of 2.8 μm [Fig. 1(a)]. The pad is 20×20 μm^2, which facilitates the magnetization switching of the LSMO nanostructures and hence DW generation. The depth of the notch (90% of the width) is about 2.5 μm, as shown in the image in Fig. 1(a). The resistance R of the structure was measured as a function of temperature T and is plotted in Fig. 1(b), verifying the metallic behavior from 400 down to 10 K. The residual resistance ratio $R_{300\,K}/R_{10\,K}$ was calculated to be 13. The Curie temperature T_c was determined to be 356 K [inset in Fig. 1(b)], close to T_c of the LSMO bulk ($\sim$360 K). We would like to point out that, due to the lack of substrate-induced strain, the notch is not expected to induce local phase separation in the LSMO nanowire, which is crucial for exploring the intrinsic effect of STT on the DW in LSMO. Otherwise, Joule heating will be generated by the applied current in the insulating region. In addition, Pt was chosen to serve as the electrical lead to build
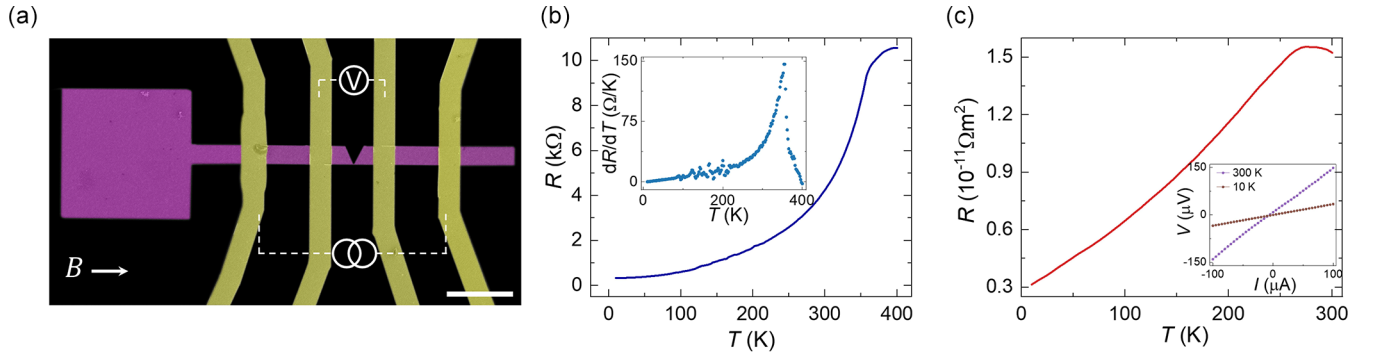
FIG. 1. (a) False-color SEM image of the notched LSMO nanostructure with a width of 2.8 μm (purple) with Pt leads (yellow). The outer two Pt leads are connected to a current source, while the inner two Pt leads serve as voltage probes. The field is always applied in plane and along the long axis of the notched LSMO nanostructure, as illustrated by the white arrow. The scale bar equals 10 μm. (b) A plot of the temperature-dependent resistance of the notched LSMO nanostructure. Inset: dR/dT versus T. T_c is determined to be 356 K. (c) Measured temperature-dependent interface resistance between the Pt leads and the notched LSMO nanostructure. Inset: Linear IV curves measured at 10 and 300 K.

a good interface contact [26]. Figure 1(c) displays a quite small resistance-area product of the interface as a function of temperature, i.e., an Ohmic contact between Pt and LSMO, as confirmed by the linear IV curves of the interface at 10 and 300 K. The interface resistance was measured in a four-probe configuration, and the area was defined as the product of the width of the Pt lead and the width of the LSMO nanowire.

We then examined the ability of DW pinning and depinning of the selected notched LSMO nanostructure with a field sweep. First, a 1 T magnetic field (in plane and along the wire) was applied to saturate the magnetization of the nanostructure at 10 K. Then, the field was decreased to +20 mT and stabilized for 1 min. The MR was recorded while the field was swept from +20 to −20 mT, that is, the major MR loop, as shown by the blue curve in Fig. 2(a). Clearly, we observe a sharp jump in MR at −6.5 mT [black arrow in Fig. 2(a)], signifying the DW was caught at the notch. We define the field of −6.5 mT as the pinning field H_{pin}. Increasing the field helped the DW to pass through the notch, resulting in a sharp drop in the major MR loop at −9.5 mT. A symmetrical MR curve was obtained when sweeping to positive fields after magnetizing the wire at −1 T. Note the fluctuation of the MR between −6.5 and −9.5 mT, which is probably due to the deformation of the DW [6]. Moreover, to show that a DW was pinned, we performed a minor loop measurement. Instead of further decreasing the field from −6.5 mT (the DW pinning field), increasing the field yielded no sharp drop in resistance in the minor MR loop and instead led to a gradual and small decrease, suggesting that the DW stayed pinned at the notch [Fig. 2(c)]. At roughly +7 mT, the MR dropped to the initial value as a result of DW depinning. We conclude that the notched structure allows controlled DW pinning and depinning. To further validate this conclusion, we performed a control experiment, for which we prepared a separate sample containing a device with a notch structure and a device without a notch. The direction of the long axis of the wire was the same for both devices. The MR behavior of the notchless device is quite different, without sharp switching behavior. Data are given in the Supplemental Material [27].

Interestingly, we also witnessed stable DW pinning and depinning at 300 K. Using the same recipe, i.e., applying a

1 T (−1 T) magnetizing field to the structure, followed by a field sweep from positive (negative) to negative (positive), the measured major MR loop unambiguously demonstrated DW pinning and depinning at 300 K, as seen in Fig. 2(b). We define the resistance of the DW as the change in resistance ΔR at the pinning and depinning fields, as indicated by the black dotted lines in Fig. 2(b). Moreover, the minor MR loop confirmed the DW was pinned stably at 300 K, in agreement with the observation at 10 K. The DW pinning and depinning at 300 K emphasize what we learned from the RT data: As shown in Fig. 1(b), even though a deep notch is introduced into the LSMO nanowire, the calculated T_c is still close to the bulk value. Notably, H_{pin} is about −0.5 mT at RT. Such a small H_{pin} enables the creation of DWs at RT in HMF LSMO, which may be applicable in relevant prototypes of devices with low power consumption.

To further unravel the DW pinning and depinning in our structures, the dependence of temperature on the magnetic behavior was investigated. As shown in Fig. 3(a), we measured the temperature dependence of ΔR and $\Delta R/R_0$ (R_0 is the resistance at zero field) of a structure with a width of 2.8 μm, extracted from the major MR loops versus temperature (see Fig. 5 in Appendix A). ΔR increases slowly with temperature from 10 to about 200 K and much faster between 200 and 300 K, while $\Delta R/R_0$ shows more variation by reaching a maximum at 100 K, followed by a minimum at 200 K. Figure 3(b) summarizes the behavior of ΔR and $\Delta R/R_0$ versus the width of the notched LSMO nanostructure based on the raw data of corresponding major MR loops (see Fig. 6 in Appendix A). Interestingly, we find an approximately constant ΔR and $\Delta R/R_0$ in the structures with a width between 5 and 1.8 μm. Pronounced increases in both ΔR and $\Delta R/R_0$ are seen in the structure with a width of 755 nm. The width of the notch in that case is less than 100 nm. Consequently, oxygen vacancies, edge dislocations, defects, etc., possibly lead to phase separation at the notch at this small size [16,19,21]. Therefore, we suspect the observed increased values may not be due to conducting LSMO. Rather, Joule heating can be generated in the insulating region subject to the current flow, hindering the efficiency of DW manipulation by STT.
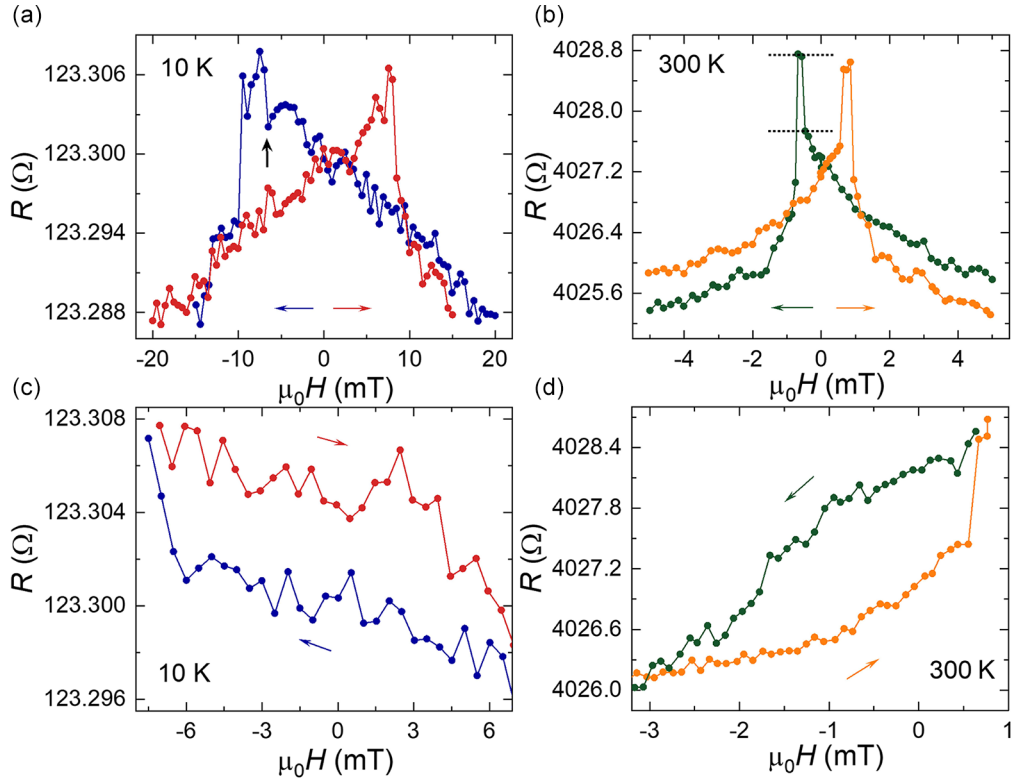
FIG. 2. (a) and (b) Major and (c) and (d) minor magnetoresistance loops of the notched LSMO nanostructure with a width of 2.8 μm, measured at 10 and 300 K, respectively. The black arrow in (a) points to the pinning field. The interval between the dotted lines in (b) defines ΔR. All other arrows indicate the field sweep directions.
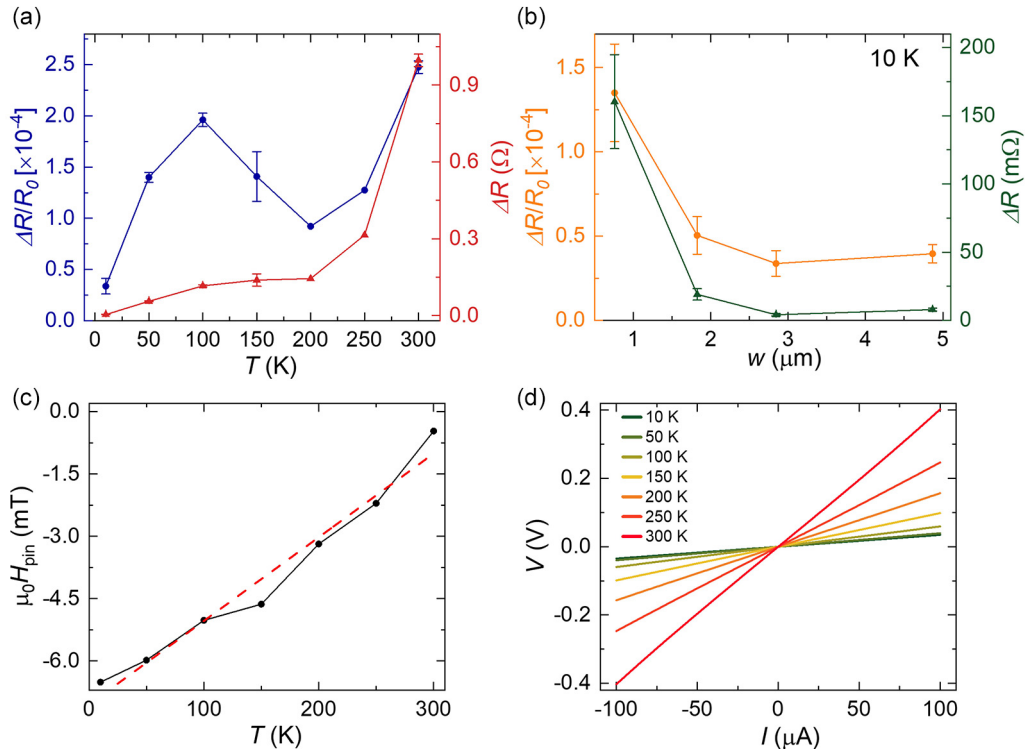

FIG. 3. (a) Temperature-dependent ΔR and $\Delta R/R_0$ of the notched LSMO nanostructure with a width of 2.8 μm. (b) At 10 K, both ΔR and $\Delta R/R_0$ remain approximately constant regardless of the widths of the notched LSMO nanostructures (from 1.8 to 5 μm), except for the case in the 755 nm LSMO nanostructure. Error bars indicate the data fluctuations. (c) The temperature-dependent DW pinning fields H_{pin} and (d) *IV* curves of the notched LSMO nanostructure with a width of 2.8 μm. The red dashed line in (c) is a linear fit.
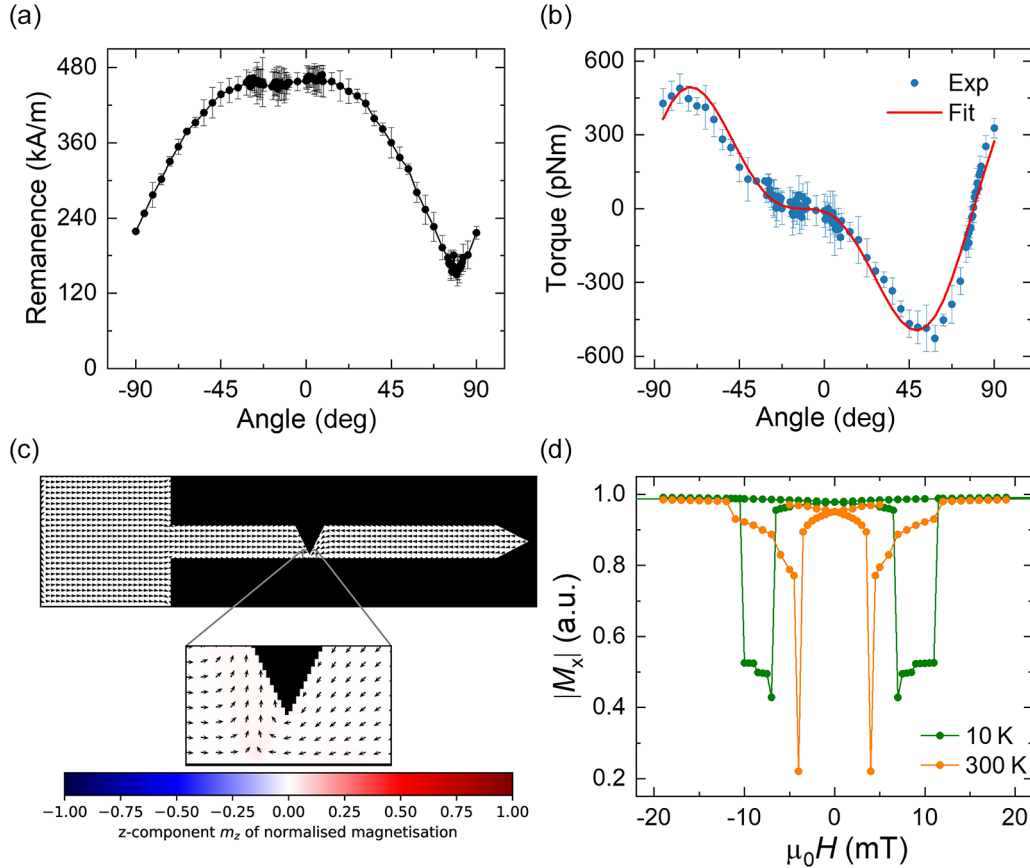
FIG. 4. (a) Dependence of the remanent magnetization on the field angle θ. (b) Extracted torque versus the angle θ of a fixed field of 20 mT. The red solid curve is the fit of the first two even terms from a Fourier series expansion. Error bars indicate the fluctuations of experimental measurements. (c) Micromagnetic simulations. Top: Magnetization state at H_{pin}, where arrows illustrate the orientations of local moments in plane, i.e., x and y components. Bottom: Magnification of the TDW at the notch. The color bar represents the z components. (d) Absolute magnetization along the long axis (x) of the notched LSMO nanostructure with a width of 3 μm at 10 K (green curve) and 300 K (orange curve).

We also inspect the temperature-dependent H_{pin} and *IV* characteristics (in the four-point geometry) of the 2.8 μm wide device [Figs. 3(c) and 3(d)], extracted from the raw data of the major MR loops at different temperatures in Fig. 5 in Appendix A. We find H_{pin} shows a nearly linear decrease with temperature, as seen by the red dashed line in Fig. 3(c). The *IV* curves of the device, measured at different temperatures, are all linear [19,20]. We conclude that the DWs we observe are different from DWs created by the insulating phase of a phase-separated nanopatterned manganite oxide [16,19,21]. This may benefit the applicability of the STT effect on the DW in HMF LSMO since, without phase separation, Joule heating in the DW can be significantly suppressed.

In order to elucidate the creation of DWs in the notched LSMO nanostructures, we performed micromagnetic simulations using the GPU-accelerated mumax3 software package [28]. The simulations require knowledge of the magnetocrystalline anisotropy of the LSMO thin films. We therefore measured the magnetization of films with thicknesses of 10 and 25 nm with a vectorial vibrating sample magnetometer [29], which allowed us to extract not only the magnetization m_x along the applied field B_x, in our case in the plane of the sample, but also the magnetization perpendicular to it and still in the plane of the

sample (m_y). In this way we measured the dependence of the remanent magnetization $m_{x,r}$ of the film as a function of the in-plane field angle θ_H, as shown in Fig. 4(a) for the 10 nm film. The measured hysteresis curves that were used to extract $m_{x,r}$ and m_y for all angles are given in the Supplemental Material [27].

Although the substrates were cut along a major crystal axis, the equipment does not allow for accurate alignment of the sample side with the magnetic field direction. Instead, we roughly defined $\theta_H = 0$ along a sample side but used the measurements to find the correct alignment of field and crystal axes. The results show a 180° periodicity, which points to a pronounced uniaxial anisotropy, characterized by an anisotropy constant K_u. The maxima and minima in the curve are shifted by about $-12°$ with respect to the supposed major axes, which was also the case for the 25 nm film (see Appendix B). We therefore redefine the in-plane field angle as $\theta_H^* = \theta_H + 12°$, making $\theta_H^* = 0$ align with a major axis. Apart from this shift, a very small dip is visible at $\theta_H^* = 0$, which is probably due to a biaxial contribution to the anisotropy (with anisotropy constant K_1). Following Ref. [22], the easy axis shifts away from the main crystal axis over an angle ϕ_{easy} and is found at the maximum in $m_{x,r}$ next to the dip. In our case this is a few degrees. The ratio K_u/K_1 equals $\cos(2\phi_{easy})$. The

error bars do not allow for an unequivocal determination of this value. However, the extracted torque signal $\tau = B_x \times m_y$, recorded at 20 mT and shown in Fig. 4(b), is more amenable to analysis. Note the field of 20 mT is optimal here to measure the magnetic torque with low noise.

As can be easily derived [30], the value of the magnetic torque exerted on the hard axis τ_{hard} equals $K_u V$, with V being the sample volume. Here, we use the aforementioned thickness of 12.5 nm as calculated from the measured saturation magnetization (0.19 ± 0.01 μA m^2) and from the theoretical value of the Mn moment ($3.8\mu_B$/f.u.). In this way, K_u is calculated to be 1634 J/m^3. We also fitted the data of the field-angle-dependent magnetic torque to the full equation for the case of both uniaxial and biaxial anisotropy:

$$\tau(\theta^*) = (K_u + K_1)\sin(2\theta^*) - 2K_1 \sin(4\theta^*). \quad (1)$$

We find that a good fit can be obtained [the red curve in Fig. 4(b)] by neglecting the K_1 term, confirming the uniaxial character of the anisotropy. The fitted K_u is about 1500 J/m^3. Therefore, we take the value for the anisotropy constant to be roughly 1600 J/m^3. We note here that we find qualitatively different magnetic anisotropy for the 25 nm film. That is not the subject of the current paper, but some comments are made in Appendix B.

With the magnetocrystalline symmetry and parameters from the above measurements, the parameters for the simulations were set at $M_s = 5.75 \times 10^5$ A/m (the saturation magnetization) and $A_{ex} = 1.7 \times 10^{-12}$ J/m (the exchange stiffness), yielding an exchange length of $\ell_{ex} \approx 2.86$ nm ($\ell_{ex} = \sqrt{2A_{ex}/\mu_0 M_s^2}$). Therefore, we set the cell size to 2 nm in the simulation to optimize the obtained results. To speed up the simulation, the damping constant was set to 0.5 instead of the intrinsic 7.4×10^{-4} [31]. The simulated DW in the notched LSMO nanostructure is displayed in Fig. 4(c). The x and y components in Fig. 4(c) are based on the simulation data and are represented by arrows. A TDW is found at the notch, as seen in the magnified image in Fig. 4(c). We calculate the width of the TDW to be 55 nm, according to $\delta = \sqrt{A_{ex}/K}$. Next, we simulated the magnetization evolution versus field, with the same recipe as that used for measuring the magnetoresistance in the experiment, i.e., magnetizing the structure by 1 T (-1 T), followed by a field sweep from 20 mT (-20 mT) to -20 mT (20 mT). The results are plotted in Fig. 4(d). At 300 K, we see the DW pining and depinning at low fields (yellow curve). As the temperature goes down to 10 K, the magnetocrystalline anisotropy becomes stronger [32]. In order to reproduce the experimental magnetoresistance measurements at 10 K in Fig. 2, in which H_{pin} is about -6.5 mT, we need a value of K_u of 4500 J/m^3. Then, the simulated H_{pin} is consistent with the experimental data, as can be seen from the simulated magnetization, plotted by the green curve. The stepped change of the magnetization between the pinning and depinning fields is due to the switching of the local spins in the TDW, i.e., DW deformation, accounting for the variation of the measured magnetoresistance of the pinned DW in Fig. 2. In total, with the extracted magnetocrystalline parameters from the field-angle-dependent measurements, the simulated DW pinning and depinning in the notched

TABLE I. Summary of the data for the DWs obtained on the notched LSMO nanostructures. Top: Pinning field H_{pin}, resistance variation ΔR, and relative resistance variation $\Delta R/R_0$ for the 2.8 μm wide structure at temperatures between 300 and 10 K. Bottom: ΔR and $\Delta R/R_0$ taken at 10 K, obtained on structures with widths varying between 0.76 and 4.9 μm.

LSMO nanostructure ($w = 2.8$ μm)			
	H_{pin} (mT)	ΔR (m Ω)	$\Delta R/R_0$ ($\times 10^{-4}$)
10 K	-6.50	4.17	0.34
50 K	-5.98	56.2	1.40
100 K	-5.02	116.3	1.96
150 K	-4.63	138.8	1.41
200 K	-3.18	144.5	0.92
250 K	-2.21	314.7	1.27
300 K	-0.47	997.1	2.48

LSMO nanostructures at 10 K		
w (μm)	ΔR (m Ω)	$\Delta R/R_0$ ($\times 10^{-4}$)
0.76	160.3	1.35
1.8	19.07	0.51
2.8	4.17	0.34
4.9	7.92	0.40

LSMO nanostructure agree quite well with our experimental observations.

IV. ON THE DW RESISTIVITY

We summarize the measured and calculated data of the notched LSMO nanostructures with a fixed length and varying widths in Table I. Knowing the DW resistance ΔR for the various widths, we now discuss the DW resistivity, defined as the resistance-area product. We calculate the area of the DW with the depth d of the notch being 90% of the width of the LSMO nanostructures with a thickness t of 10 nm and the DW resistivity according to $\rho_{DW} = td\Delta R$. At 300 K, the DW resistivity of the structure with a width of 2.8 μm is 2.8×10^{-15} Ω m^2, consistent with the reported large-area-averaged intrinsic DW resistivity in LSMO [33], but now measured on a single DW. At 10 K, we obtain 3.4×10^{-17}, 1.1×10^{-17}, and 3.8×10^{-17} Ω m^2 for the structures with widths of 1.8, 2.8, and 4.9 μm, respectively. For $w = 755$ nm, the DW resistivity is about 1.6×10^{-16} Ω m^2.

To put this in perspective, in an early experiment on a macroscopic LSMO sample with many domains, grown on LaAlO$_3$, the DW resistivity was estimated to be of the order of 10^{-15} Ω m^2 at 300 K [34]. At the same time, measurements on a structured LCMO sample with many constrictions gave a value of 8×10^{-14} Ω m^2 at 77 K [35]. Later, Arnal *et al.* reported an even larger value of 2.5×10^{-13} Ω m^2 at 8 K in an LSMO wire connected to two pads by notchlike structures [19]. It was remarked that this value is significantly higher than what is generally found in 3d metals, where values are rather in the range 10^{-17}–10^{-18} Ω m^2. This discrepancy may be attributed to the contribution of anisotropic magnetoresistance and colossal magnetoresistance to the measured DW resistance in the experiments [36]. In the case of an

overconstricted LSMO nanostructure, metallic and insulating regions may coexist and give rise to extrinsic DW resistance, i.e., overestimated DW resistivity [19]. Bakaul *et al.* reported the estimated intrinsic DW resistivity of LSMO to be $1.9 \times 10^{-15} \, \Omega \, m^2$, averaged by characterizing stripe domains [33]. For our single DW, we find similar values of around $10^{-15} \, \Omega \, m^2$ at 300 K, decreasing to on the order of $10^{-17} \, \Omega \, m^2$ at 10 K.

V. CONCLUSIONS

In this work, we demonstrated stable DW pinning and depinning in a notched LSMO nanostructure with a width of $2.8 \, \mu m$ at temperatures between 10 and 300 K by recording both the major and minor MR loops while sweeping the magnetic field. There is no apparent contribution of phase separation to the observed DW creation and annihilation, as verified by the high T_c (356 K) and the linear IV curves taken at different temperatures. The absolute value of the pinning field H_{pin} was found to increase linearly with decreasing temperature. In particular, a DW can be created by a very small field (-0.5 mT) at 300 K, promising low-power consumption application at RT. Moreover, analyzing the temperature-dependent ΔR and $\Delta R/R_0$, we found that both reach a maximum at 300 K. Varying the width of the notched LSMO nanostructure from 1.8 to 4.9 μm, we did not observe a pronounced change in ΔR and $\Delta R/R_0$ at 10 K, except for the case of 755 nm. With the magnetocrystalline parameters extracted from the field-angle-dependent measurements, our micromagnetic simulations show that a TDW is confined at the notch. The simulated evolution of magnetization of the LSMO nanostructure agrees well with our experimental observations. Additionally, we found the DW

resistivity to be on the order of $10^{-17} \, \Omega \, m^2$ at 10 K and $10^{-15} \, \Omega \, m^2$ at 300 K. The latter value is in agreement with the reported intrinsic DW resistivity at 300 K. The results emphasize, once more, that the DW resistivity in this half-metallic ferromagnet is not qualitatively different from the values found in $3d$ ferromagnetic metals. The stable DW pinning and depinning may guide future investigations of the STT effect on metallic DWs with spin-polarized currents and may promote the progress of relevant spintronic applications.

DATA AVAILABILITY

The data that support the findings are available from the corresponding author upon reasonable request.

APPENDIX A: DW PINNING AS FUNCTION OF TEMPERATURE

We collected major MR loops at different temperatures, as partly shown in Fig. 5. Obviously, DW pinning and depinning are present, as a sign of jump and drop in the MR curves. We extract and discuss ΔR, $\Delta R/R_0$, and H_{pin} in the main text.
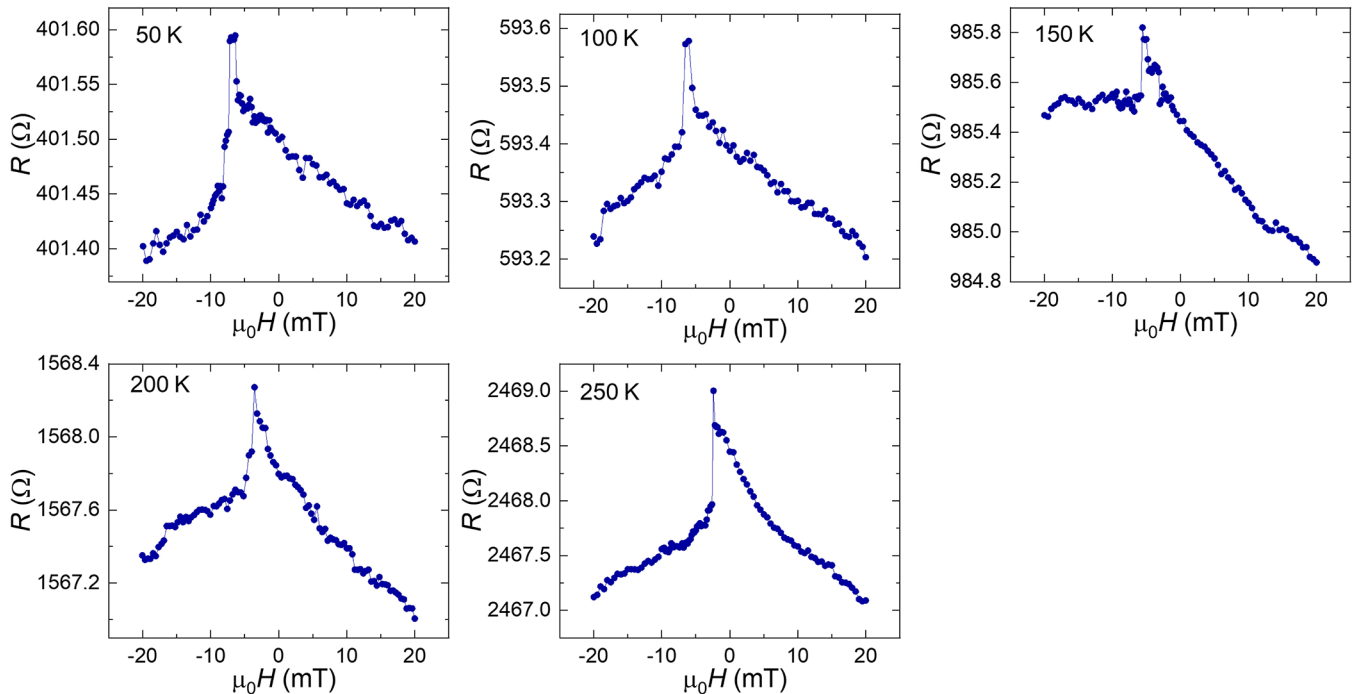

FIG. 5. Positive-to-negative-field part of major MR loops of the notched LSMO nanostructure with a width of 2.8 μm, taken at different temperatures. DW pinning and depinning are seen from 50 to 250 K.
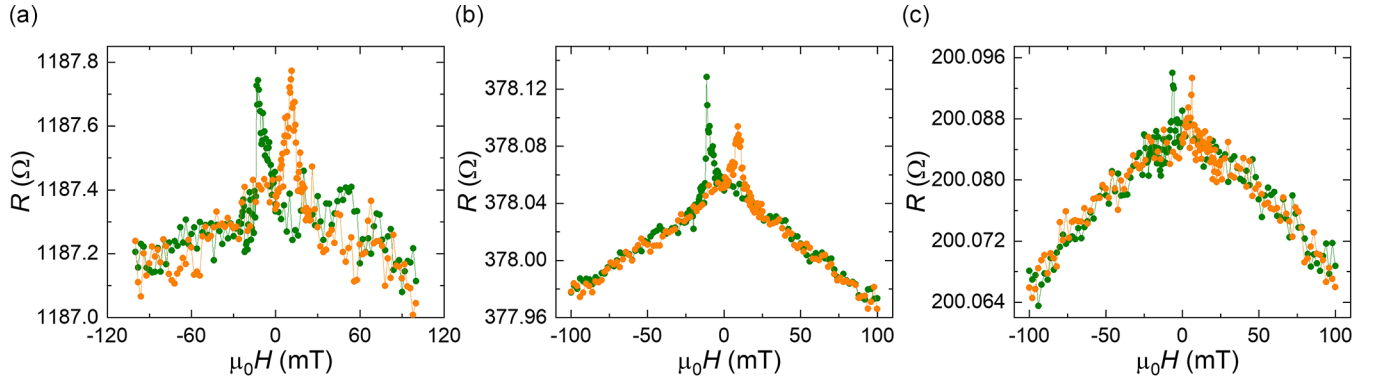
FIG. 6. Major MR loops of the notched LSMO nanostructures with a width of (a) 0.76 μm, (b) 1.8 μm, and (c) 4.9 μm, measured at 10 K.

The dependence of the various dimensions on DW pinning and depinning is summarized in Fig. 6. At 10 K, we conducted major MR measurements on notched LSMO nanostructures with widths of 755 nm [Fig. 6(a)], 1.8 μm [Fig. 6(b)], and 4.9 μm [Fig. 6(c)]. Together with ΔR and $\Delta R/R_0$ obtained for the 2.8 μm wide LSMO nanostructure in the main text, we summarize all the values extracted from the results shown in Fig. 6 and plotted in Fig. 3 in the main text. We find approximately constant ΔR and $\Delta R/R_0$ in notched LSMO nanostructures with a width larger than 2 μm. The discrepancy in the 0.76 μm wide LSMO nanostructure can probably be attributed to phase separation.

APPENDIX B: TORQUE MEASUREMENTS OF THE MAGNETIZATION

The remanent magnetization of an LSMO film with a thickness of 12.5 nm is recorded and plotted in Fig. 4(a), where we mention an offset in the angle of the field with the major crystal axes. Qualitatively, the film shows a periodicity of 180° in the remanent magnetization, indicative of uniaxial anisotropy.

Interestingly, the magnetocrystalline anisotropy of an LSMO film with a thickness of 25 nm shows quite different behavior. As shown in Fig. 7(a), a nearly 90° periodicity is

found in the angle-dependent remanent magnetization, revealing a pronounced biaxial anisotropy here. The minimum is found at −12°, which is roughly the same offset that we found for the 12.5 nm film. Taking that offset into account, the maxima in the remanence, reflecting the direction of the easy axes, are found at $\theta_H^* = \pm 54°$. This is the typical behavior of a mixture of uniaxial and biaxial magnetic anisotropy. The torque versus angle, measured in fields of 9 mT (yellow), 12 mT (green), and 20 mT (brown), is plotted in Fig. 7(b) and gives a similar picture. Taking the maximum of the torque, K_u is calculated to be 850 J/m³, which is smaller than that of the LSMO film with a thickness of 12.5 nm. Fitting the data for the torque versus angle of a field of 9 mT to Eq. (1) now requires both the K_u and K_1 terms, yielding comparable K_u and K_1 of 280 and 330 J/m³, respectively. For this work, in which we focus on the DW pinning and depinning, a thickness of about 10 nm, with rather strong uniaxial anisotropy, is more favorable for DW manipulation [37].

One cautionary remark should be made. We observe uniaxial anisotropy at small thicknesses, changing to more biaxial anisotropy at higher thicknesses. This was observed before for LSMO on LSAT [32,38] and was attributed to interface- and substrate-related effects that disappear with thickness. However, the opposite was also found, in which a thin film (12 nm) showed biaxial anisotropy while a thicker one (40 nm) was
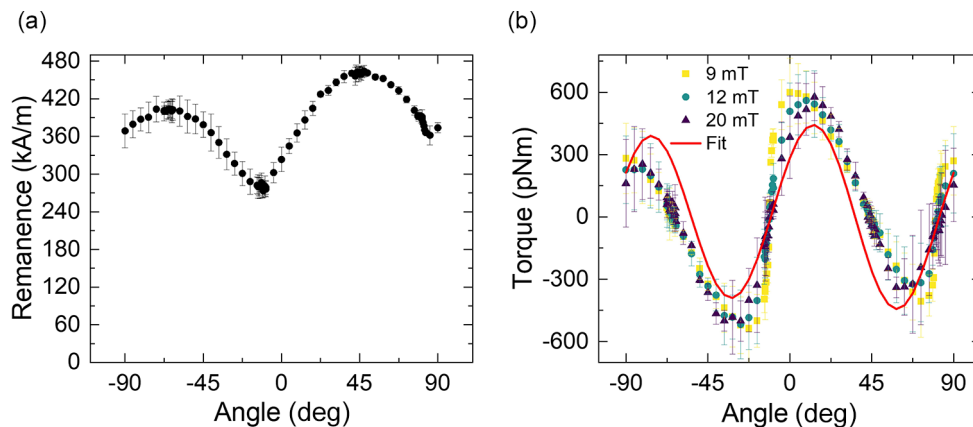

FIG. 7. (a) Dependence of the remanent magnetization on the field angle θ of an LSMO film with a thickness of 25 nm. (b) Plots of the extracted torque versus the angle θ of a field of 9 mT (yellow), 12 mT (green), and 20 mT (brown). The red curve is the fit to Eq. (1).

uniaxial [22]. Clearly, the substrate quality and the growth conditions play a crucial role in determining the magnetic behavior. In both cited experiments, the growth method was pulsed laser deposition. We used off-axis sputtering, with a very low growth rate, which is probably the major factor in the behavior we observe.

[1] Y. Zhang, J. Liu, Y. Dong, S. Wu, J. Zhang, J. Wang, J. Lu, A. Rückriegel, H. Wang, R. Duine *et al.*, Strain-driven Dzyaloshinskii-Moriya interaction for room-temperature magnetic skyrmions, Phys. Rev. Lett. **127**, 117204 (2021).

[2] R. Fermin, D. Van Dinter, M. Hubert, B. Woltjes, M. Silaev, J. Aarts, and K. Lahabi, Superconducting triplet rim currents in a spin-textured ferromagnetic disk, Nano Lett. **22**, 2209 (2022).

[3] S. S. P. Parkin, M. Hayashi, and L. Thomas, Magnetic domain-wall racetrack memory, Science **320**, 190 (2008).

[4] A. Fernández-Pacheco, R. Streubel, O. Fruchart, R. Hertel, P. Fischer, and R. P. Cowburn, Three-dimensional nanomagnetism, Nat. Commun. **8**, 15756 (2017).

[5] J. Shibata, G. Tatara, and H. Kohno, A brief review of field- and current-driven domain-wall motion, J. Phys. D **44**, 384004 (2011).

[6] M. Hayashi, L. Thomas, C. Rettner, R. Moriya, X. Jiang, and S. S. P. Parkin, Dependence of current and field driven depinning of domain walls on their structure and chirality in permalloy nanowires, Phys. Rev. Lett. **97**, 207205 (2006).

[7] J.-S. Kim, M.-A. Mawass, A. Bisig, B. Krüger, R. M. Reeve, T. Schulz, F. Büttner, J. Yoon, C.-Y. You, M. Weigand *et al.*, Synchronous precessional motion of multiple domain walls in a ferromagnetic nanowire by perpendicular field pulses, Nat. Commun. **5**, 3429 (2014).

[8] S. Fukami, M. Yamanouchi, S. Ikeda, and H. Ohno, Depinning probability of a magnetic domain wall in nanowires by spin-polarized currents, Nat. Commun. **4**, 2293 (2013).

[9] R. Moriya, L. Thomas, M. Hayashi, Y. B. Bazaliy, C. Rettner, and S. S. P. Parkin, Probing vortex-core dynamics using current-induced resonant excitation of a trapped domain wall, Nat. Phys. **4**, 368 (2008).

[10] M. Hayashi, L. Thomas, R. Moriya, C. Rettner, and S. S. P. Parkin, Current-controlled magnetic domain-wall nanowire shift register, Science **320**, 209 (2008).

[11] A. Yamaguchi, T. Ono, S. Nasu, K. Miyake, K. Mibu, and T. Shinjo, Real-space observation of current-driven domain wall motion in submicron magnetic wires, Phys. Rev. Lett. **92**, 077205 (2004).

[12] G. Tatara, H. Kohno, and J. Shibata, Microscopic approach to current-driven domain wall dynamics, Phys. Rep. **468**, 213 (2008).

[13] W. Chen, L. Qian, and G. Xiao, Resistance of domain-wall states in half-metallic CrO_2, Phys. Rev. B **98**, 174402 (2018).

[14] A. Biehler, M. Kläui, M. Fonin, C. König, G. Güntherodt, and U. Rüdiger, Domain structures and the influence of current on domains and domain walls in highly spin-polarized CrO_2 wire elements, Phys. Rev. B **75**, 184427 (2007).

[15] A. Vailionis, H. Boschker, W. Siemons, E. P. Houwman, D. H. A. Blank, G. Rijnders, and G. Koster, Misfit strain accommodation in epitaxial ABO_3 perovskites: Lattice rotations and lattice modulations, Phys. Rev. B **83**, 064101 (2011).

[16] A. Ruotolo, A. Oropallo, F. Miletto Granozio, G. P. Pepe, P. Perna, U. S. Di Uccio, and D. Pullini, Current-induced domain wall depinning and magnetoresistance in $La_{0.7}Sr_{0.3}MnO_3$ planar spin valves, Appl. Phys. Lett. **91**, 132502 (2007).

[17] J. Wang, L. S. Xie, C. S. Wang, H. Z. Zhang, L. Shu, J. Bai, Y. S. Chai, X. Zhao, J. C. Nie, C. B. Cao *et al.*, Magnetic domain-wall motion twisted by nanoscale probe-induced spin transfer, Phys. Rev. B **90**, 224407 (2014).

[18] J. Wang, S. Wu, J. Ma, L. Xie, C. Wang, I. A. Malik, Y. Zhang, K. Xia, C.-W. Nan, and J. Zhang, Nanoscale control of stripe-ordered magnetic domain walls by vertical spin transfer torque in $La_{0.67}Sr_{0.33}MnO_3$ films, Appl. Phys. Lett. **112**, 072408 (2018).

[19] T. Arnal, A. V. Khvalkovskii, M. Bibes, B. Mercey, P. Lecoeur, and A.-M. Haghiri-Gosnet, Electronic properties of domain walls in $La_{2/3}Sr_{1/3}MnO_3$: Magnetotransport measurements on a nanopatterned device, Phys. Rev. B **75**, 220409(R) (2007).

[20] C. Beekman, J. Zaanen, and J. Aarts, Nonlinear mesoscopic transport in a strongly cooperative electron system: The $La_{0.67}Sr_{0.33}MnO_3$ microbridge, Phys. Rev. B **83**, 235128 (2011).

[21] L. Marín, L. Morellón, P. A. Algarabel, L. A. Rodríguez, C. Magén, J. M. De Teresa, and M. R. Ibarra, Enhanced magneto-transport in nanopatterned manganite nanowires, Nano Lett. **14**, 423 (2014).

[22] H. Boschker, M. Mathews, P. Brinks, E. P. Houwman, A. Vailionis, G. Koster, D. H. A. Blank, and G. Rijnders, Uniaxial contribution to the magnetic anisotropy of $La_{0.67}Sr_{0.33}MnO_3$ thin films induced by orthorhombic crystal structure, J. Magn. Magn. Mater. **323**, 2632 (2011).

[23] C. Yin, D. Krishnan, N. Gauquelin, J. Verbeeck, and J. Aarts, Controlling the interfacial conductance in $LaAlO_3/SrTiO_3$ in $90°$ off-axis sputter deposition, Phys. Rev. Mater. **3**, 034002 (2019).

[24] Y. Junxiang, P. Kumar, M. Cabero-Piris, and J. Aarts, Nonlocal spin transport based on a half-metallic ferromagnet, Phys. Rev. Mater. **7**, 104408 (2023).

[25] J. Crangle and G. M. Goodman, The magnetization of pure iron and nickel, Proc. R. Soc. A **321**, 477 (1971).

[26] M. Abuwasib, H. Lee, A. Gruverman, C.-B. Eom, and U. Singisetti, Contact resistance to $SrRuO_3$ and $La_{0.67}Sr_{0.33}MnO_3$ epitaxial films, Appl. Phys. Lett. **107**, 242905 (2015).

[27] See Supplemental Material at http://link.aps.org/supplemental/10.1103/np4m-j4b7 for additional details on the magnetization measurements, and for data on a device without a notch.

[28] A. Vansteenkiste, J. Leliaert, M. Dvornik, M. Helsen, F. Garcia-Sanchez, and B. Van Waeyenberge, The design and verification of MuMax3, AIP Adv. **4**, 107133 (2014).

[29] J. Rigue, D. Chrischon, A. M. H. De Andrade, and M. Carara, A torque magnetometer for thin films applications, J. Magn. Magn. Mater. **324**, 1561 (2012).

[30] B. Dodrill, J. Lindemuth, and J. Krause, Magnetic anisotropy: Measurements with a vector vibrating sample magnetometer, application note (Lake Shore Cryotronics, Westerville, Ohio). See also J. Burd, M. Huq and E. W. Lee, J. Magn. Magn. Mat. **5**, 135 (1977).

[31] Q. Qin, S. He, W. Song, P. Yang, Q. Wu, Y. P. Feng, and J. Chen, Ultra-low magnetic damping of perovskite $La_{0.7}Sr_{0.3}MnO_3$ thin films, Appl. Phys. Lett. **110**, 112401 (2017).

[32] S. K. Chaluvadi, Influence of the epitaxial strain on magnetic anisotropy in LSMO thin films for spintronics applications, Ph.D. thesis, Normandie Université, 2017.

[33] S. R. Bakaul, W. Hu, T. Wu, and T. Kimura, Intrinsic domain-wall resistivity in half-metallic manganite thin films, Phys. Rev. B **86**, 184404 (2012).

[34] Y. Wu, Y. Suzuki, U. Rüdiger, J. Yu, A. D. Kent, T. K. Nath, and C.-B. Eom, Magnetotransport and magnetic domain structure in compressively strained colossal magnetoresistance films, Appl. Phys. Lett. **75**, 2295 (1999).

[35] N. D. Mathur, P. B. Littlewood, N. K. Todd, S. P. Isaac, B.-S. Teo, D.-J. Kang, E. J. Tarte, Z. H. Barber, J. E. Evetts, and M. G. Blamire, Resistance of a domain wall in $La_{0.7}Sr_{0.3}MnO_3$, J. Appl. Phys. **86**, 6287 (1999).

[36] M. Ziese, Extrinsic magnetotransport phenomena in ferromagnetic oxides, Rep. Prog. Phys. **65**, 143 (2002).

[37] M. T. Bryan, S. Bance, J. Dean, T. Schrefl, and D. A. Allwood, Transverse and vortex domain wall structure in magnetic nanowires with uniaxial in-plane anisotropy, J. Phys.: Condens. Matter **24**, 024205 (2012).

[38] S. K. Chaluvadi, F. Ajejas, P. Orgiani, S. Lebargy, A. Minj, S. Flament, J. Camarero, P. Perna, and L. Méchin, Epitaxial strain and thickness dependent structural, electrical and magnetic properties of $La_{0.67}Sr_{0.33}MnO_3$ films, J. Phys. D **53**, 375005 (2020).